ROYAL SOCIETY
OF CHEMISTRY

PAPER

Quantitative elemental mapping of chondritic meteorites using laser ablation-inductively coupled plasma-time of flight-mass spectrometry (LA-ICP-TOF-MS)†

Ryoga Maeda, [ID] *ab Thibaut Van Acker, [ID] c Frank Vanhaecke, [ID] c
Akira Yamaguchi, [ID] d Vinciane Debaille,b Phillippe Claeys [ID] a and Steven Goderis [ID] a

Fast elemental mapping using laser ablation-inductively coupled plasma-time of flight-mass spectrometry (LA-ICP-TOF-MS) was applied to a set of chondritic meteorite samples, more specifically H chondrites. LA-ICP-TOF-MS enables element distribution maps for both major and trace elements to be obtained at μm-order spatial resolution (5 × 5 μm square pixels in this study) in a (semi-)quantitative manner. To assess the reliability of the quantitative data as obtained using LA-ICP-TOF-MS mapping, the accuracy and precision as obtained using this fast elemental mapping approach were compared to those of the data obtained using the more conventional spot analysis with an electron probe micro analyzer and LA-ICP-sector field (SF)-MS for major and trace elements, respectively. The maps obtained using LA-ICP-TOF-MS visualize elemental distributions among the constituent minerals, while major and trace element abundances determined using LA-ICP-TOF-MS are overall in good agreement within up to 30% relative uncertainty with those obtained based on the spot analyses and with literature values. Yet, some analytical limitations of LA-ICP-TOF-MS mapping remain due to the limited ablated yield when using a small laser spot size for high spatial resolution mapping, while ICP-TOF-MS shows a lower sensitivity and narrower linear dynamic range than does ICP-SF-MS. On the other hand, the main host phase(s) of an element can be readily identified and the major and trace element abundances in the phase(s) can be quantified with an accuracy approaching that of the spot analyses. As such, this study demonstrates the potential of LA-ICP-TOF-MS for fast quantitative imaging of various types of samples, in particular geological samples.

Introduction

In situ spot analysis and elemental mapping in geological and geochemical research are commonly based on electron probe micro analysis (EPMA), scanning electron microscopy in combination with energy-dispersive X-ray spectrometry, micro-X-ray fluorescence spectrometry (μXRF), or secondary ion mass spectrometry (SIMS). Most of these techniques are valuable in the context of major element concentrations (generally >0.1% m m^{-1} level) for both spot analysis and mapping, but their application is more limited in relation to trace element analysis due to

their relatively high limits of detection. For the determination of trace elemental abundances, laser ablation-inductively coupled plasma-mass spectrometry (LA-ICP-MS) is now widely used as a direct solid sampling micro-analytical technique.[1–3] The LA-ICP-MS technique not only determines the trace elemental abundances in mineral phases, but also provides spatially resolved information in the form of elemental maps for major, minor, and trace elements.[4,5] Recently, hardware developments focusing on low-dispersion ablation cells and aerosol transport systems, which reduce the duration of single pulse response profiles and boost the signal-to-noise ratio and speed of analysis, significantly improved the analytical capabilities of LA-ICP-MS elemental mapping.[6,7] Moreover, the launch of commercially available time-of-flight (TOF) based ICP-mass spectrometers, providing rapid quasi-simultaneous detection of nearly the entire elemental mass spectrum for each individual laser pulse, has boosted the use of LA-ICP-MS for elemental mapping applications in a wide variety of research fields. ICP-TOF-MS instruments can handle the short transient signals produced with low-dispersion LA setups and provide fast multi-elemental detection in contrast to sequential scanning-type ICP-mass

aAnalytical-, Environmental-, and Geo-Chemistry, Vrije Universiteit Brussel, Pleinlaan 2, 1050 Brussels, Belgium. E-mail: Ryoga.Maeda@vub.be

bLaboratoire G-Time, Université libre de Bruxelles, CP 160/02, 50, Av. F. D. Roosevelt, 1050 Brussels, Belgium

cAtomic & Mass Spectrometry (A&MS) Research Unit, Department of Chemistry, Ghent University, Campus Sterre, Krijgslaan, 281 – S12, 9000 Ghent, Belgium

dNational Institute of Polar Research, 10-3 Midori-cho, Tachikawa-shi, Tokyo 190-8518, Japan

† Electronic supplementary information (ESI) available. See DOI: https://doi.org/10.1039/d2ja00317a

This journal is © The Royal Society of Chemistry 2023

J. Anal. At. Spectrom., 2023, **38**, 369–381 | **369**

spectrometers such as quadrupole (Q) or sector field (SF)-based mass analyzers.[7–10] TOF-based mass analyzers have also been developed for SIMS.[11,12] TOF-SIMS and LA-ICP-TOF-MS are complementary in terms of mapping: TOF-SIMS is capable of achieving a higher spatial resolution at the order of tens of nm and a higher depth resolution, but with a limited range in terms of analysis area up to about tens of μm, while LA-ICP-TOF-MS is capable of handling mm-cm ranges of analysis area with μm-order spatial resolution. To reveal elemental distributions among the constituent minerals in geological samples in a (semi-)quantitative manner, LA-ICP-TOF-MS is preferred due to the larger range of analysis area (cm order) and significantly lower matrix effects than TOF-SIMS.

Meteorites are divided into two major categories, chondritic and non-chondritic meteorites based on their bulk compositions and textures.[13] Chondritic meteorites generally consist of chondrules embedded in a very fine-grained matrix (<5 μm). LA-ICP-TOF-MS mapping is an ideal tool for studying such samples because their elemental distributions among the constituent minerals, especially in the case of trace elements, remain poorly understood due to the small size of minerals. To date, however, the application of LA-ICP-TOF-MS to geological samples has been yet limited.[10,14–23] In addition, the technique has so far been applied to meteorite samples in few studies.[15] Therefore, in this study, LA-ICP-TOF-MS mapping is applied to a set of H group of ordinary chondrites (H chondrites), which are the most abundant of all meteorite classes (∼40% by number: based on the Meteoritical Bulletin Database, **https://www.lpi.usra.edu/meteor/metbull.php**, accessed 27 September 2022), with the aim of assessing the potential of state-of-the-art LA-ICP-TOF-MS instrumentation in terms of speed, spatial resolution, LODs, and accuracy and precision. For this purpose, the quantitative data obtained were compared with those using more conventional EPMA and LA-ICP-SF-MS spot drilling approaches.

Experimental

Samples

The same polished thick sections (PTSs) as those studied in Maeda *et al.* (2021)[24] were used for the analyses described below. Additionally, PTSs for Jilin (H5), Nuevo Mercurio (H5), Richardton (H5), and Butsura (H6) were allocated by the Royal Belgian Institute of Natural Sciences (RBINS), Belgium, and prepared for these analyses. Petrographic information on the meteorite samples is listed in Table 1. Note that for reasons of conciseness, only the results for two samples, A 09618 (H5) and Y-790960 (H7) out of the larger 16-sample collection, are shown in this fundamental study.

LA-ICP-TOF-MS mapping

Prior to LA-ICP-TOF-MS mapping, all PTSs were analyzed using a Bruker M4 Tornado μXRF scanner equipped with a Rh source and two XFlash 430 Silicon Drift detectors at the Vrije Universiteit Brussel (VUB), Belgium, to obtain major element maps. These analyses have been described in detail in Maeda *et al.* (2021).[24] The PTSs of 12 samples (A-880941, A-881258, A 09436, A 09387, NWA 6771, Jilin, Nuevo Mercurio, Richardton, A 09618,

Table 1 List of chondritic meteorite samples analyzed in this study (n.d.: not determined)[a]

Meteorite	Type	Weathering
A-880941	H3.3	A/B
Y-793574	H3.5	n.d.
Y-790461	H3.7	B
ALH 78084	H3.9	B/Ce
A-881258	H3.9[b]	B
A 09436	H3	C
A 09387	H4	B/C
NWA 6771	H4	W1
Jilin	H5	n.d.
Nuevo Mercurio	H5	n.d.
Richardton	H5	n.d.
A 09618	H5	C
Sahara 97035	H5	W2
Butsura	H6	n.d.
A 09516	H6	C
Y-790960	H7	B

[a] See Maeda *et al.* (2021)[24] for the details of the type and weathering index. [b] Ninagawa *et al.* (2005).[25]

Butsura, A 09516, and Y-790960) were analyzed using pulse-resolved multi-elemental LA-ICP-TOF-MS mapping at Ghent University, Belgium. Two LA-units equipped with a 193 nm ArF* excimer-based nanosecond lasing system were used: a customized Teledyne Photon Machines Analyte G2 and a commercially available Teledyne Photon Machines Iridia LA-unit equipped with a prototype and commercially available version of the cobalt ablation chamber, respectively. Both systems were equipped with low-dispersion tube cell-type ablation cells.[6,7,26,27] The LA-units were coupled to a TOFWERK icpTOF 2R ICP-TOF-MS unit equipped with a 1 mm inner diameter torch injector *via* a low-dispersion aerosol transport system, named "aerosol rapid introduction system" (ARIS), developed at Ghent University, and commercialized by Teledyne Photon Machines.[28] The instrumental setups provide fast quasi-simultaneous detection across almost the entire elemental mass range (14–256 amu), which is highly beneficial for pulse-resolved multi-elemental mapping applications as mentioned above.[9,15,29] Daily tuning of the instrument settings and data acquisition conditions was performed while ablating NIST SRM 612 glass reference material aiming at low laser-induced elemental fractionation ($^{238}U^+/^{232}Th^+ \approx 1$), high sensitivity across the elemental mass range and low levels of oxide formation ($^{238}U^{16}O^+/^{238}U^+ < 0.5\%$). All instrument settings and data acquisition conditions for the fast LA-ICP-TOF-MS mapping approach are listed in Table 2.

The regions of interest for LA-ICP-TOF-MS mapping were selected based on the major element X-ray maps. For each sample, these X-ray maps were imported into Chromium v2.7, the operating software of the LA-unit, and were aligned to the live camera view, *i.e.*, to the actual position and orientation of the samples in the ablation chamber. For quantification purposes, 13 external calibration standards (MPI-DING glass reference materials: ATHO-G, GOR128-G, KL2-G, ML3B-G, StHs6/80-G, and T1-G; USGS glass reference materials: BCR-2G, BHVO-2G, BIR-1G, GSD-1G, GSE-1G, and NKT-1G; and in-

Table 2 Instrument settings and data acquisition conditions for LA-ICP-TOF-MS mapping.

Analyte G2 and Iridia LA-units	
Laser energy density (J cm^{-2})	4.00
Repetition rate (Hz)	100 or 200[a]
Spot size (μm)	5
Mask shape	Square
Lateral scan speed (μm s^{-1})	500 or 1000[a]
He carrier gas flow rate (L min^{-1})	0.50

icpTOF 2R ICP-mass spectrometer	
RF power (W)	1580
Ar plasma gas flow rate (L min^{-1})	15
Ar auxiliary gas flow rate (L min^{-1})	0.90
Ar make-up gas flow rate (L min^{-1})	0.96
Integrated TOF spectra per data point	103–206

[a] Either 100 Hz with 500 μm s^{-1} or 200 Hz with 1000 μm s^{-1} for the repetition rate and the lateral scan speed.

house Durango apatite) were analyzed before and after mapping the regions of interest in the meteorite samples. Ablation was performed according to consecutive edge-to-edge line scans over regions of interest of 1–10 mm^2 using a square laser spot size of 5 × 5 μm and the data/pixel acquisition rate was matched to the laser repetition rate of either 100 or 200 Hz.

The elemental mass spectra were recorded using the TOF-WERK Tofpilot v2.8 software and stored in HDF5 files, an open-source hierarchal data format. The data analysis package Tofware v3.1.1 was used for data post-processing including time-dependent mass calibration, modeling and subtracting baseline signal intensities, and peak shape determination and integration.[30] Subsequently, Teledyne HDIP software v.1.6 was used for further data post-processing steps, such as external calibration based on a sum normalization approach and exporting the quantitative elemental maps.[31] Once the quantitative elemental maps were obtained, each constituent mineral in a sample was systematically identified using "clustering zones", which is a k-means clustering algorithm automatically identifying the phases based on the levels of selected elements in the HDIP software. Given the constituent minerals in H chondrites, the automatic clustering was performed based on the following elements: Na, Mg, Al, Si, P, S, Ca, Sc, Ti, Cr, and Fe. Images identified using the automatic clustering approach are shown in Fig. 4 and discussed together with the results of the elemental maps. Note that two phosphate phases in the meteorite samples, apatite and merrillite, were masked manually because the clustering did not effectively distinguish between these phases. Finally, the elemental abundances in the constituent minerals were determined by taking an average of the elemental abundances in the corresponding

regions. To avoid matrix effects as much as possible, especially in the case of the phosphate phases, phases of silicates, phosphates, and the others were differently calibrated using all the MPI-DING and USGS glasses, the Durango apatite only, and all the MPI-DING and USGS glasses combined with the Durango apatite, respectively. The following nuclides were used for the quantification: ^{23}Na, ^{24}Mg, ^{27}Al, ^{28}Si, ^{31}P, ^{39}K, ^{43}Ca, ^{45}Sc, ^{49}Ti, ^{51}V, ^{52}Cr, ^{55}Mn, ^{57}Fe, ^{59}Co, ^{60}Ni, ^{63}Cu, ^{66}Zn, ^{85}Rb, ^{88}Sr, ^{89}Y, ^{137}Ba, ^{90}Zr, ^{93}Nb, ^{139}La, ^{140}Ce, ^{141}Pr, ^{143}Nd, ^{147}Sm, ^{153}Eu, ^{157}Gd, ^{159}Tb, ^{163}Dy, ^{165}Ho, ^{167}Er, ^{169}Tm, ^{173}Yb, ^{175}Lu, ^{178}Hf, ^{181}Ta, ^{208}Pb, ^{232}Th, and ^{238}U. BHVO-2G, GOR128-G, and the Durango apatite were also quantified using the same procedures for the validation of this analysis. Incidentally, BHVO-2G and GOR128-G were calibrated as silicate phase while the Durango apatite was calibrated as phosphate phase.

Electron probe microanalysis

First, all the samples to be analyzed using LA-ICP-TOF-MS were slightly polished and subjected to the following analyses. Back-scattered electron (BSE) images of all PTSs were generated using a JEOL JSM-7100F field emission-scanning electron microscope (FE-SEM) equipped with an Oxford energy-dispersive spectrometer at the National Institute of Polar Research (NIPR), Japan. By combining the BSE images with the X-ray maps obtained using μXRF, the constituent minerals in the samples were identified. Based on the constituent minerals identified, the major and minor elemental abundances of the constituent minerals in the PTSs were determined using a JEOL JXA-8200 electron micro probe analyzer at the NIPR. All analyses were carried out using a 15 kV accelerating voltage. Different measurement conditions were used depending on the mineral phase, and these conditions are listed in Table 3. Counting times ranged from 10 to 100 s on peaks for each mineral. Correction procedures are based on the ZAF method. As a result of the occurrence of overlapping signals, the intensity of V was mathematically corrected for the intensity of Ti. Natural and synthetic silicates, oxides, and metals with well-known chemical compositions were used as standards. A fluorapatite standard was used for the quantification of F.

Spot drilling analysis using LA-ICP-SF-MS

The trace element abundances of Ca-phosphates and silicates in the samples were determined using LA-SF-ICP-MS in single-point drilling mode. These measurements were performed using a Teledyne CETAC LSX-213 G2+ LA-system coupled to a Thermo Element XR ICP-SF-MS unit at the NIPR. The laser system provides an output wavelength of 213 nm and 100 shots were fired per spot analysis at a laser repetition of 10 Hz and a laser energy density of 36 J cm^{-2}. Oxide formation was set to a low level by tuning the parameters while ablating NIST SRM 612 glass reference material (^{232}Th^{16}O$^+$/^{232}Th$^+$ < 0.5%). All nuclide peaks were collected at low mass resolution ($M/\Delta M = \sim300$) with triple mode detection and the following nuclides were monitored for the major elements: ^{23}Na, ^{24}Mg, ^{27}Al, ^{29}Si, ^{31}P, ^{39}K, ^{43}Ca, ^{44}Ca, and ^{57}Fe; and for the trace elements: ^{45}Sc, ^{51}V, ^{55}Mn, ^{66}Zn, ^{85}Rb, ^{88}Sr, ^{89}Y, ^{137}Ba, ^{139}La, ^{140}Ce, ^{141}Pr, ^{146}Nd, ^{147}Sm, ^{151}Eu, ^{157}Gd, ^{159}Tb, ^{161}Dy, ^{165}Ho, ^{166}Er, ^{169}Tm, ^{173}Yb, ^{175}Lu, ^{178}Hf, ^{208}Pb, ^{232}Th, and ^{238}U. All peaks were acquired by peak jumping between peak tops

This journal is © The Royal Society of Chemistry 2023

J. Anal. At. Spectrom., 2023, **38**, 369–381 | **371**

Table 3 EPMA experimental conditions for each mineral phase.

Mineral phase	Beam current (nA)	Beam size (μm)	Monitored elements
Phosphate	5	5	F, Na, Ma, Si, P, Cl, Ca, and Fe
Olivine, pyroxene, and oxide	30	<1	Na, Mg, Al, Si, P, Ca, Ti, V, Cr, Mn, Fe, Ni, and Zn
Feldspar	10	<1 or 1	Na, Mg, Al, Si, P, K, Ca, Ti, Cr, Mn, and Fe

Table 4 Experimental conditions of each mineral phase for LA-ICP-SF-MS spot analysis.

Mineral phase	Spot size (μm)	Monitored major elements	Monitored trace elements
Phosphate	10–100	Mg, Al, Si, P, Ca, Mn, and Fe	V, Rb, Sr, Y, Ba, REEs, Hf, Pb, Th, and U
Pyroxene	30–100	Mg, Al, Si, P, Ca, and Fe	Sc, Zn, Rb, Sr, Y, Ba, REEs, Hf, Pb, Th, and U
Feldspar and olivine	50–100	Na, Mg, Al, Si, P, K, Ca, Mn, and Fe	Zn, Rb, Sr, Y, Ba, REEs, Hf, Pb, Th, and U

with 10% mass window (average of 5 peaks on the peak top) and 50–100 milliseconds of acquisition time on the peak top. Depending on the target phase, nuclides monitored were selected among those mentioned above and laser spot sizes were selected so that detectable intensities were obtained, especially in the case of the rare earth elements (REEs). This information is summarized in Table 4.

Elemental abundances were calculated using average relative sensitivity factors (RSFs) obtained from triplicate analysis of the in-house Durango apatite for phosphate phases (except for Rb and Hf) and BCR2-G, BHVO2-G, and ML3B-G for all other phases as well as for Rb and Hf in phosphate phases.[32] For phosphate and silicate phases, elemental abundances obtained based on EPMA were used as an internal standard, either P or Ca, Si or Ca, Al or Si, and Si or Fe for phosphate, pyroxene, feldspar, and olivine phases, respectively. When the laser purely ablated the target mineral grain without any overlap with other phases, there was no resolvable difference in the abundances calculated between both internal standards. Thus, in this case, Ca, Al, and Fe were used as the internal standard for phosphate and pyroxene, feldspar, and olivine phases, respectively. However, the signals from these internal standards were in some subject spectrally overlapping with signals from major elements of other phases (e.g., the ablation on the edge between two phases). In these cases, the other element was used as the internal standard for the corresponding phases if the effects of the overlap on the internal element and the trace elements were negligible. Specifically, the effects were considered negligible in case there was <10% discrepancy with the data obtained upon ablation of the corresponding pure phases in which the major elemental abundances obtained are in good agreement with those obtained based on EPMA. Any data points showing a larger discrepancy were discarded. Consequently, the number of data points for some phases is limited, even though at least three grains per phase were analyzed for each sample. The precision and accuracy of each analysis were confirmed via analysis of the ATHO-G, GOR128-G, and GOR132-G reference materials using the same quantitative procedures.

Results and discussion

Assessment of quantification using LA-ICP-TOF-MS mapping and LA-ICP-SF-MS spot analysis

The elemental abundances in the reference materials determined using LA-ICP-TOF-MS mapping are listed in ESI Table 1,†
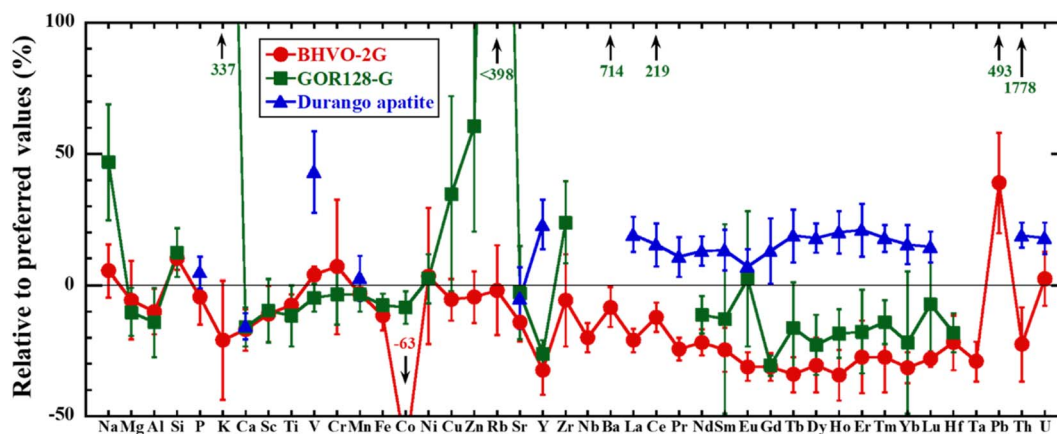

Fig. 1 Bias (%) between the elemental abundances in reference materials obtained using LA-ICP-TOF-MS mapping and the corresponding preferred values (see ESI Table 1† for the details of the comparison values).[34–37] The error bars represent 1 SD.

together with their preferred or reference values and limits of detection (LODs) for each analysis point calculated using the IUPAC approximation formula.[33] Overall, elements contained in the material at more than 0.1% m m^{-1} level are within ~10% relative uncertainty (RU) and those at µg g^{-1} level are within ~20% RU. Most elemental abundances obtained for BHVO-2G and GOR128-G and those in the Durango apatite agree within ~30% and ~20% of their preferred and reference values, respectively (Fig. 1). In most cases in which the preferred or reference values were close to the LOD, the abundances obtained display a larger discrepancy from their comparison value (>20%). For example, in the case of K in GOR128-G, the LOD is 0.01% m m^{-1}, the preferred value is 0.030% m m^{-1}, and the value obtained is 0.13% m m^{-1}. Such a large discrepancy is also observed for Co in BHVO-2G and Ba, Ce, Pb, and Th in GOR128-G. Except for Co in BHVO-2G, all other values displaying such discrepancy are significantly higher than the preferred values and exhibit a large RU up to ~70%. Even though the signals of these elements monitored were above the LOD, the preferred values, *i.e.*, the actual values of these elements in GOR128-G are overall below the LOD and thus their abundances are considered unreliable, causing the observed discrepancy.

The trace element abundances in the reference materials obtained using LA-ICP-SF-MS spot analysis (hereafter LA-spot analysis) are listed in ESI Table 2,† together with their preferred values and LOD values (3 SD). On average, the RU for each analysis is up to ~15% although Th and U in GOR128-G and GOR132-G, which are present at the level of less than tens of ng g^{-1}, display relatively high RUs (~20–85%). Compared with their preferred values, most elemental abundances determined overlap within uncertainty (Fig. 2). A relatively large discrepancy between the obtained and preferred value is observed for Pb in ATHO-G and Th and U in GOR132-G determined using the pyroxene analysis condition (~50% differences from the preferred values). Especially in the case of

Th in GOR132-G, the ratio of the LOD value to the preferred value is one of the largest values at ~5% while those of the other elements in all other analyses are less than 1%, which is similar to those obtained for LA-ICP-TOF-MS mapping in terms of those ratios. However, different from LA-ICP-TOF-MS mapping, all the values obtained with a large discrepancy are lower than the preferred values and none of the values obtained exceeding their preferred values display more than a 30% difference.

Based on the assessment of accuracy and precision of the quantitative procedure for LA-ICP-TOF-MS mapping and LA-spot analysis described above, the RU of elemental abundances in unknown samples obtained using LA-ICP-TOF-MS mapping identified as phosphate phases, all other phases, and LA-spot analysis can be estimated at 30%, 20%, and 15%, respectively. These RUs estimated are applied to the following results.

Quantitative elemental mapping of meteorites using LA-ICP-TOF-MS

Fig. 3 shows an optical image for Y-790960 (H7) after being ablated for LA-ICP-TOF-MS mapping and a combined semi-quantitative element map for Y-790960 in RGB (Ca, Si, and Fe, respectively) obtained using LA-ICP-TOF-MS mapping. Metal and sulfide phases occur as bright (white) areas in Fig. 3(a). As such, the region ablated for LA-ICP-TOF-MS mapping obviously contains these metal and sulfide phases. However, the metal phase was not successfully ablated by the nanosecond laser pulses and thus some black regions are visible in Fig. 3(b), while the other phases including sulfide were ablated properly. Fig. 4 shows combined RGB elemental maps and quantitative elemental maps for A 09618 (H5) together with the corresponding optical and BSE images and images identified for individual mineral phases using the automatic clustering approach. When comparing Fig. 4(a)–(d), all phases including the metal phase in the region of interest appear to have been
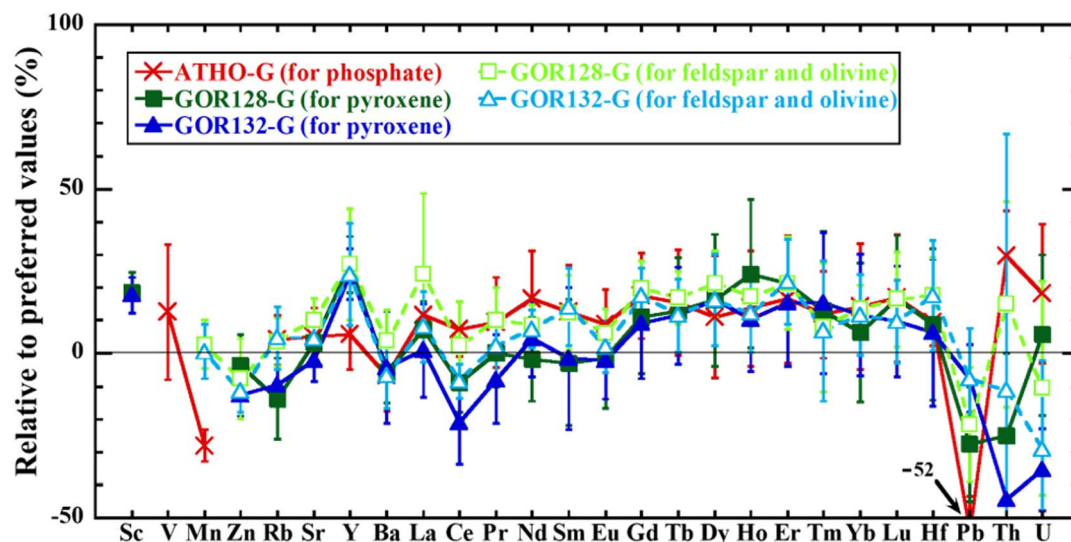

Fig. 2 Bias (%) between the elemental abundances in reference materials obtained using LA-ICP-SF-MS spot analysis and the corresponding preferred values.[35] The error bars represent 1 SD.

This journal is © The Royal Society of Chemistry 2023

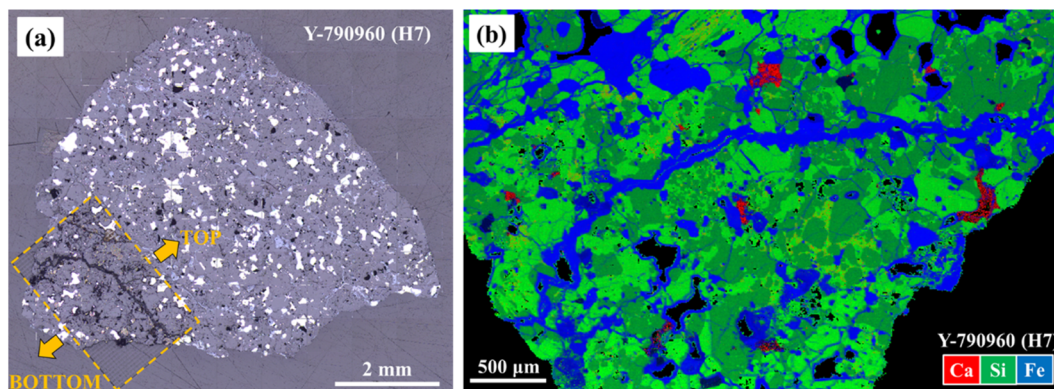*J. Anal. At. Spectrom.*, 2023, **38**, 369–381 | **373**

Fig. 3 Optical image with the region analyzed using LA–ICP–TOF–MS mapping indicated by a broken orange rectangle (a) and a combined semi-quantitative element map obtained using LA–ICP–TOF–MS mapping (b) for meteorite Y-790960. The element map is shown in RGB (red: Ca, green: Si, and blue: Fe) and the color brightness in the RGB map indicates their abundance level as higher abundance is brighter.

ablated successfully. This successful ablation of the metal phase may be due to the metal phase in this sample being oxidized or hydrated by terrestrial weathering to some degree. Therefore, all elemental maps obtained with the experimental conditions selected for LA-ICP-TOF-MS mapping in this study do not contain metal phases unless these phases are oxidized or hydrated.

Fig. 3(a) shows that the region analyzed using LA-ICP-TOF-MS retains some traces of the ablation as the contrast of this region is different from that of the non-ablated area. However, no effects of this damage are observed upon BSE imaging (Fig. 4(b)). In addition, there are no resolvable differences in the elemental abundances within the minerals as obtained using EPMA and LA-spot analysis, following prior ablation. While the effects resulting from ablation of LA-ICP-TOF-MS mapping in this study appear limited based on BSE imaging, EPMA, and LA-spot analysis, optical and detailed petrographic observations using FE-SEM may indicate minor but discernible effects. In contrast, with the applied experimental condition for LA-ICP-TOF-MS mapping, pure metal was not ablated. As thermal diffusion in metal phases occurs more rapidly than in the other phases, the laser energy density was likely not sufficient to ablate metal. Although ablating the metal phase at higher laser energy density (7–8 J cm^{-2}) was attempted, the ablation of the metal phase remained ineffective. On the other hand, metal phases in iron meteorites were successfully ablated at a significantly higher laser energy density of 36 J cm^{-2} using the Teledyne CETAC LSX-213 G2+ nanosecond LA-system at the NIPR.[38] However, this approach may result in total ion counts that exceed the detector's linear dynamic signal range of the icpTOF 2R (6 orders of magnitude), as the highest total ion count already reached 10^5 cps level with the experimental conditions used in this study. Furthermore, ablation with such a high energy density increases the degree of damage to the selected region of interest for LA-ICP-TOF-MS mapping, resulting in apparent effects for subsequent BSE imaging, EPMA, and LA-spot analysis.

Fig. 5 shows combined elemental maps for Y-790960. Fig. 4(c) and 5(a) exhibit their combined Ca, Mg, and Si maps,

allowing identification of Ca-phosphates, Ca-rich pyroxene, low-Ca pyroxene, feldspar, and olivine. Chromite, metal, sulfide phases can be distinguished based on the Cr, Fe and S abundances in Fig. 4(d) as these appear in reddish orange, green, and bright blue, respectively. As such, the constituent minerals in the meteorite samples are readily identified using major element maps obtained based on LA-ICP-TOF-MS mapping. Fig. 4(e) and (f) display the results of the automatic clustering approach for individual mineral phases (i.e., olivine and low-Ca pyroxene, respectively), as applied during the quantitative procedure. Based on Fig. 4(b) and (c), the automatic clustering zones are highly efficient at identifying the individual target silicate phases. This is a significant advantage of LA-ICP-TOF-MS mapping in terms of obtaining representative elemental abundances for the target phase, because the elemental abundances obtained using LA-ICP-TOF-MS mapping were averaged with as many grains as contained in the region analyzed, while conventional spot analysis usually provides those averaged based on a few grains only, especially in the case of trace element analysis. Combined, Fig. 4(c), (h), (j), 5(a), (b) and (d) demonstrate that REEs and U are concentrated in Ca-phosphate phases, with REEs mainly hosted in merrillite and U in apatite. Scandium and Hf are largely distributed in Ca-rich pyroxene according to Fig. 4(c), (g) and (i). Based on Fig. 5(c), Nb is highly concentrated in a phase identified as ilmenite. These observations are entirely consistent with previously determined elemental distributions and partition coefficients.[39–42] Therefore, LA-ICP-TOF-MS mapping provides adequate elemental distributions not only of major elements but also of trace elements, at least in their main host phase(s). Surprisingly, a significant fraction of the REEs and U reside in the crack displayed in Fig. 4, almost at the same concentration levels as those observed in merrillite. A similar deposition was confirmed in other samples analyzed in this study (A 09436, A 09387, NWA 6771, Nuevo Mercurio, and A 09516). This distribution is also consistent with chemical leaching experiments,[43] in which REEs, Th, and U have been deduced to reside in cracks and along grain boundaries. These depositions in cracks likely result from terrestrial weathering because most meteorite

374 | J. Anal. At. Spectrom., 2023, 38, 369–381

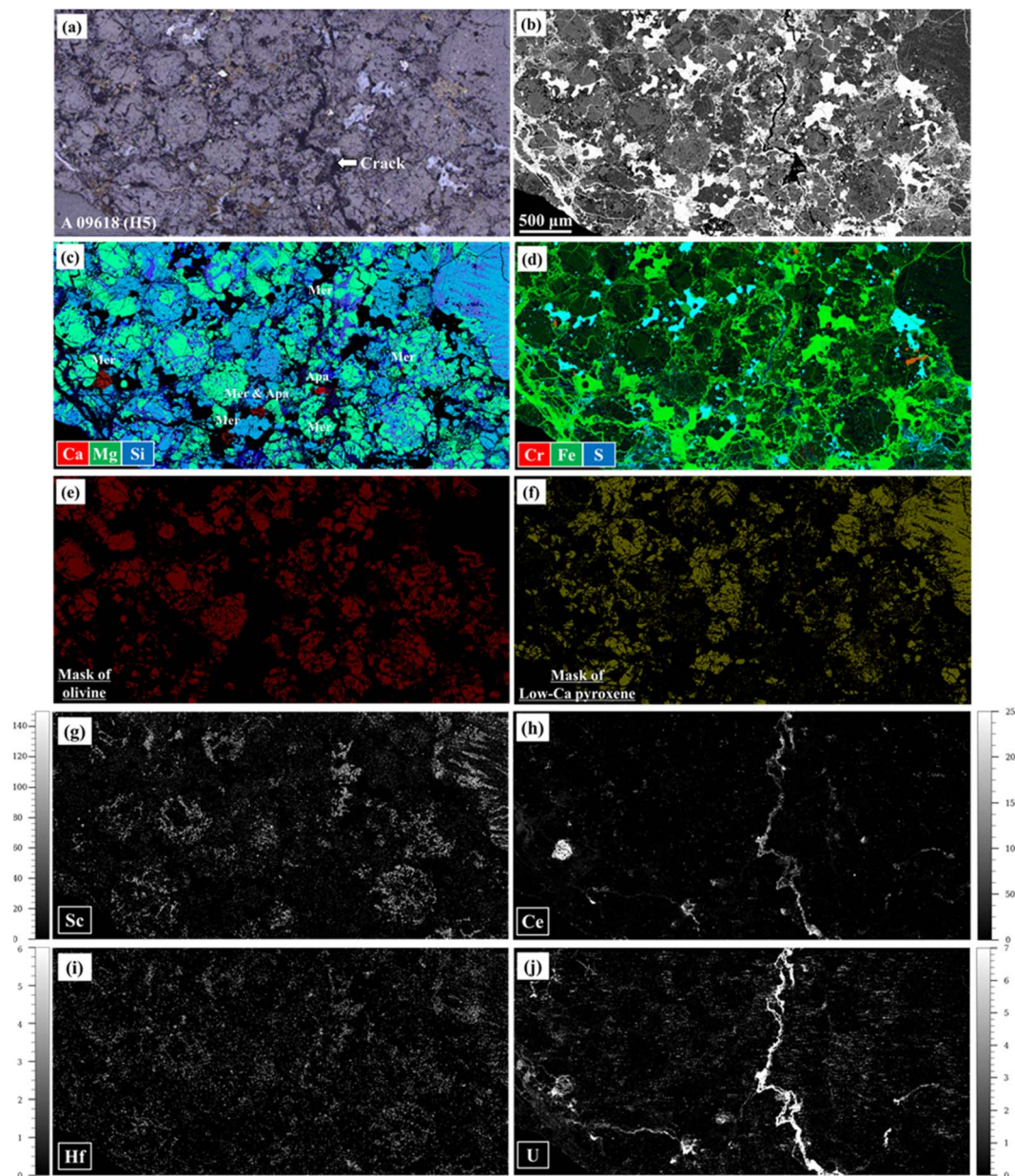This journal is © The Royal Society of Chemistry 2023

Fig. 4 Optical and BSE images, individual mineral phase images after clustering, and (semi-)quantitative element maps for meteorite A 09618. (a) Optical image of the region analyzed using LA-ICP-TOF-MS. (b) BSE image of the region analyzed using mapping. (c) Combined RGB elemental map obtained using LA-ICP-TOF-MS mapping with red: Ca, green: Mg, and blue: Si. Based on the composition, the following mineralogy can be deduced red: Ca-phosphates (Mer: merrillite; Apa: chlorapatite), light green: olivine, light blue: low-Ca pyroxene, blue: feldspar, and violet: Ca-rich pyroxene. (d) Combined RGB elemental map with red: Cr, green: Fe, and blue: S. (e) Olivine phase identified using the automatic clustering. (f) Low-Ca pyroxene phase masked using the automatic clustering. (g) Scandium distribution map. (h) Cerium distribution map. (i) Hafnium distribution map. (j) Uranium distribution map. Scale bars for (g)–(j) in µg g^{-1}.

samples displaying such depositions are heavily weathered (Table 1). The trace element mapping using LA-ICP-TOF-MS reported here represents the first instance in which such depositions are visually confirmed, and as such LA-ICP-TOF-MS mapping demonstrates the capability to determine elemental distributions in cracks and along grain boundaries where conventional spot analyses cannot be applied readily.

As demonstrated by Fig. 4(g), (h), 5(c) and (d), quantitative elemental maps were obtained using LA-ICP-TOF-MS. The

elemental abundances for the whole area studied in A 09618 and Y-790960 as determined using LA-ICP-TOF-MS mapping are listed in ESI Table 3,† together with their bulk rock values and H chondrite mean values as a comparison.[24,44] In the following, only the results for A 09618 and Y-790960 are described and discussed in detail as representative examples. The trends in all other obtained data sets are similar to those in the selected meteorites. In comparison with the corresponding bulk rock values and the H chondrite mean values (Fig. 6), most elemental
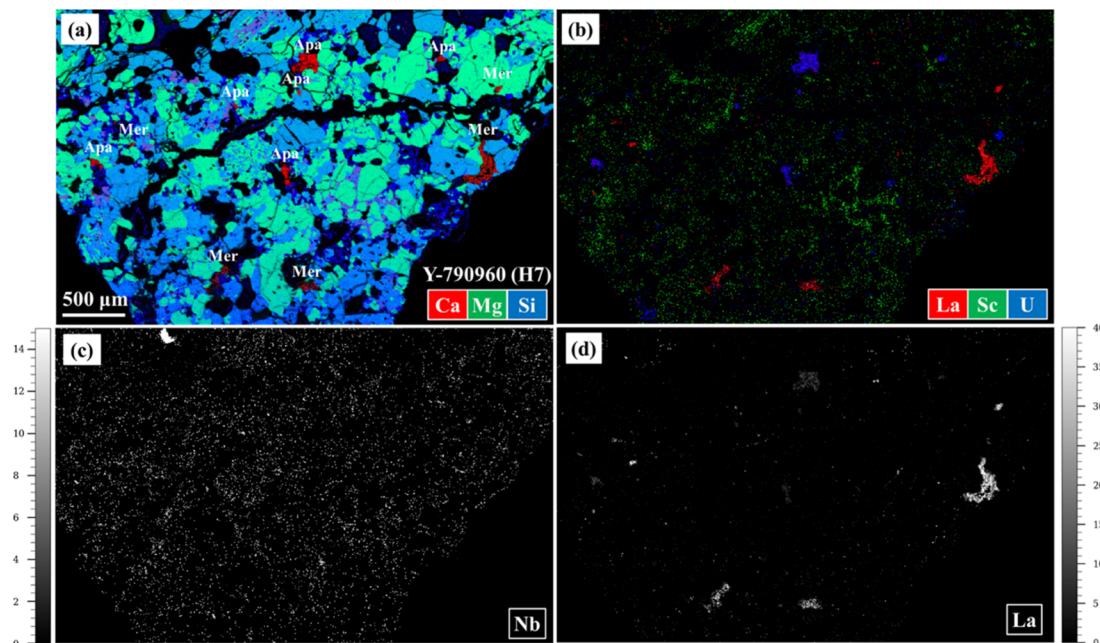
This journal is © The Royal Society of Chemistry 2023

J. Anal. At. Spectrom., 2023, **38**, 369–381 | 375

Fig. 5 (Semi-)quantitative element maps for meteorite Y-790960. (a) Combined RGB elemental map with red: Ca, green: Mg, and blue: Si. Based on the composition, the following mineralogy can be deduced, red: Ca-phosphates (Mer: merrillite; Apa: chlorapatite), light green: olivine, light blue: low-Ca pyroxene, blue: feldspar, and violet: Ca-rich pyroxene. (b) Combined RGB elemental map with red: La, green: Sc, and blue: U. (c) Niobium distribution map. (d) Lanthanum distribution map. Scale bars for (c) and (d) in μg g^{-1}.
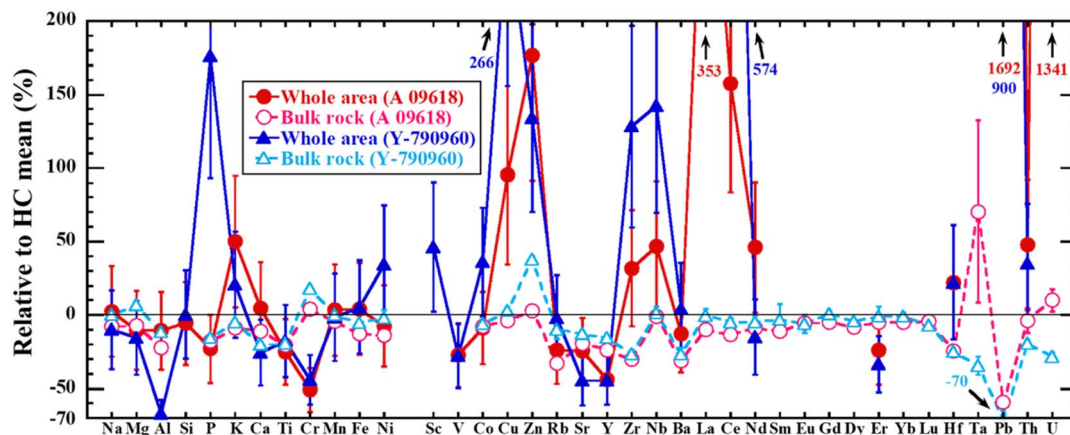
Fig. 6 Bias (%) between the elemental abundances in the whole area of the meteorite samples as obtained using LA-ICP-TOF-MS mapping and the corresponding bulk rock values after compared to HC mean values. Bulk rock values and HC mean values are from Maeda *et al.* (2021) and Wasson and Kallemeyn (1988).[24,44] The error bars for the whole areas represent 30% relative uncertainty.

abundances obtained agree within uncertainty with them although REEs abundances were mostly below the corresponding LODs. A large discrepancy between the obtained and comparison values is systematically observed for Cr, Cu, Zn, Ce, Pb, and U in both samples. In addition, La in A 09618 and Al, P, Zr, and Nb in Y-790960 disagree with the comparison values. As meteorite samples, especially chondrites, are highly heterogeneous compared with the glass and apatite reference materials used for the data validation, heterogeneity at the scale of the whole areas analyzed likely causes these discrepancies. As such, the discrepancies for Al, P, and Cr observed may reflect

a heterogeneous distribution of their corresponding host minerals in the samples studied because these elements are one of the major elements constituting feldspar, phosphate, and chromite, respectively. The lower abundance of Sr and the value below the LOD for Eu, largely accommodated in feldspar, in Y-790960 correspond to the lower Al abundance, while the abundances of V, largely partitioned in chromite, in both samples are depleted similar to the Cr abundances.[39,40] Thus, the discrepancies for Al in Y-790960 and Cr in both samples should be related to a heterogeneous distribution of feldspar and chromite, respectively. In the case of P, a region containing

376 | *J. Anal. At. Spectrom.*, 2023, **38**, 369–381

This journal is © The Royal Society of Chemistry 2023

relatively abundant Ca-phosphates in the sample was selected for LA-ICP-TOF-MS mapping to see the effect on the REE distribution, likely leading to the high P abundance observed in Y-790960. Based on LA-ICP-TOF-MS mapping, Zr and Nb are highly concentrated in ilmenite (Fig. 5(c)), hence the discrepancies for these elements in Y-790960 may result from a heterogeneous distribution of this accessory phase. The discrepancy for La in A 09618 may be explained by the deposition in cracks as mentioned above, given that the U abundance in this sample is significantly higher than the comparison values. For the other elements displaying discrepancies (Cu, Zn, Ce, Pb, and U), similarly high abundances are obtained in the other meteorite samples analyzed in this study systematically. The too high results for Pb and U are attributed to their actual abundances being below the corresponding LODs. In the cases of Cu, Zn, and Ce, the signals obtained may have been elevated by matrix or memory effects. Incidentally, it is also possible that the anomalously high Zn and Pb abundances are caused by contamination on the surface of the PTSs.
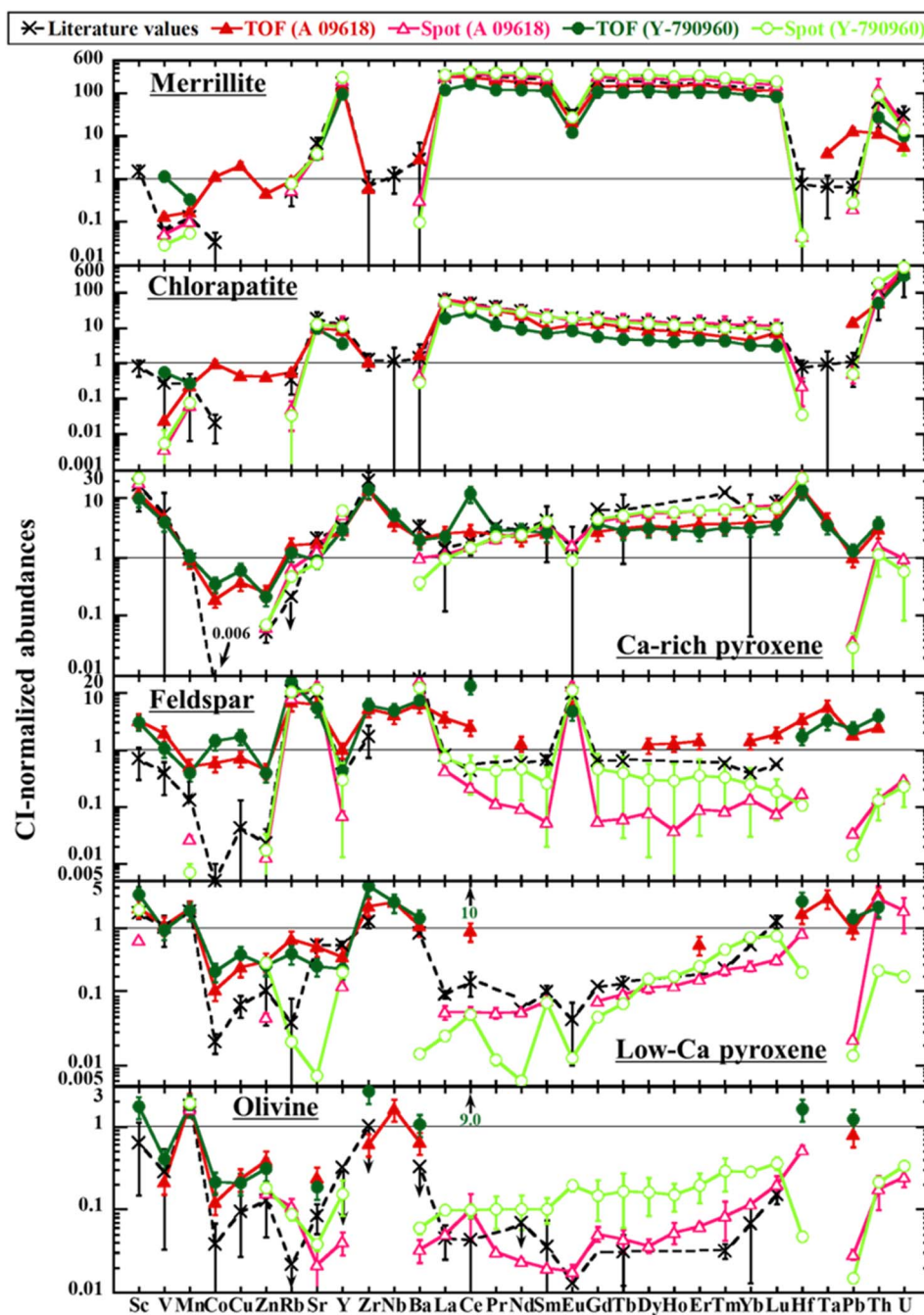

Fig. 7 CI-normalized abundances of trace elements in constituent minerals as obtained using LA-ICP-TOF-MS mapping (TOF) and LA-ICP-SF-MS spot analysis (spot) to the corresponding literature values.[39,40,42,45,46] See ESI Tables 4–9† for the details on the uncertainties. Error bars may be smaller than the symbol size. CI values are from Anders and Grevesse (1989).[47]

Comparison of elemental abundances in constituent minerals

The elemental abundances in the Ca-phosphate, silicate, and oxide phases for A 09618 and Y-790960 determined using LA-ICP-TOF-MS mapping and spot analyses of EPMA and LA-ICP-SF-MS are summarized in ESI Tables 4–10,† together with literature values compiled from Ward *et al.* (2017) for Ca-phosphates and Mason and Graham (1970), Allen and Mason (1973), Curtis (1974), and Curtis and Schmitt (1979) for the other phases.[39,40,42,45,46] Here, the elemental abundances obtained for each phase and those compiled are shown in Fig. 7, with the exception of the oxide phases, and compared for each phase one by one. Note that the clustering of mineral phases during the quantitative procedure on LA-ICP-TOF-MS mapping in some cases covers other phases than the target phase to a minor degree. This is attributed to ablation of tiny inclusions smaller than the laser spot size (5×5 μm) together with the target phase or to overlap with (an)other phase(s) during the ablation of the rim of the target phase. Moreover, particularly in the case of weathered samples, such samples may contain narrow Fe-rich veins within mineral grains (*e.g.*, Fig. 4), which are also ablated together with the target phase. As such, each phase identified may contain analyzed points of non-target phases, affecting some of the elemental abundances in the phase as if contaminated by other phases. As an example, the Fe abundances in low-Fe phases such as Ca-phosphates and feldspar and the Co abundances in all phases determined are systematically elevated as the result of overlap with (oxidized or hydrated) metal phases (ESI Tables 4–10†). Especially the effects of metal phases on the Fe abundances in low-Fe phases can significantly modify the major element abundances following the applied 100% normalization, as all Fe is calculated as FeO. Similar effects may influence the values used for reference. For example, Ward *et al.* (2017) determined the major and trace element abundances in Ca-phosphates for several types of meteorites using EPMA, SIMS, and LA-spot analyses.[42] As they mostly focused on REE abundances, the abundances of other trace elements less concentrated in Ca-phosphates such as Ba and Hf may be affected by overlap with other phase(s), *e.g.*, resulting from ablating a phase underneath the target phase. The authors themselves note that the Pb abundances in some samples are possibly affected by contamination issues. In case of the elements systematically displaying a discrepancy for the whole areas mentioned above (Cu, Zn, Ce, Pb, and U), the abundances in constituent minerals determined using LA-ICP-TOF-MS mapping display a similar discrepancy from the comparison values overall. Because most of these elemental abundances obtained using LA-ICP-TOF-MS mapping show constant values (*e.g.*, ~100 μg g^{-1} for Cu and Zn), which are higher than the comparison values in all phases and their bulk rock values, these discrepancies should be attributed to matrix/memory effects or contamination affecting the entire area. Especially in the case of Pb, all abundances determined using LA-ICP-TOF-MS mapping appear to be affected by contamination. These effects must be considered during the following comparisons.

Merrillite. The major element abundances determined using EPMA are in excellent agreement with their literature values,

while most of those determined using LA-ICP-TOF-MS mapping display slight discrepancies from the literature values (ESI Table 4†). In terms of trace elements (ESI Table 4† and Fig. 7), the Ba, Hf, and Pb abundances determined using LA-spot analysis are significantly lower than the literature values, which suggests that the literature values of Ba and Hf suffer from simultaneously sampling other phases as noted above. The high literature value of Pb must result from terrestrial contamination.[41] The other trace element abundances determined using LA-spot analysis overlap within uncertainty with the literature values. The Th and U abundances determined using LA-ICP-TOF-MS mapping display values remarkably lower than those obtained using LA-spot analysis, while the V and Ta abundances are higher than previously reported values. The Th and U discrepancies for the LA-ICP-TOF-MS values may occur because Th and U are more heterogeneously distributed in merrillite than the other elements as a result of their limited mobility. The high V and Ta abundances obtained using LA-ICP-TOF-MS mapping are either influenced by neighboring phases or caused by values too close to the corresponding LODs, especially in the case of Ta, as merrillite is one of the phases showing the lowest abundances of these elements. However, overall, the CI-normalized abundance patterns for LA-ICP-TOF-MS mapping, LA-spot analysis, and literature values overlap with each other. In particular, the REE abundance patterns are rich in light REEs (LREEs) relative to the heavy REEs (HREEs) and display a negative Eu anomaly. All Th/U ratios overlap within uncertainty, despite the discrepancies in their abundances observed between LA-ICP-TOF-MS mapping and LA-spot analysis.

Apatite. Based on the major element abundances determined using EPMA, apatite contains ~5% m m^{-1} of Cl and ~0.5% m m^{-1} of F, confirming it is chlorapatite. This is consistent with the literature values in ESI Table 5† and what is currently known about apatite in ordinary chondrites.[48] The major element abundances as determined using LA-ICP-TOF-MS mapping are affected by overlap with other phases (mostly metal phases) as the data obtained are slightly higher than the literature values (ESI Table 5†). In terms of trace elements, the V, Mn, Rb, and Ba abundances determined using LA-spot analysis are lower than the reported literature values (ESI Table 5† and Fig. 7). Similar to merrillite, the literature values may be elevated due to overlap with neighboring phases. Although the REE abundances in Y-790960 as obtained using LA-ICP-TOF-MS mapping are lower than the literature values, the CI-normalized REE patterns for LA-ICP-TOF-MS mapping, LA-spot analysis, and literature values agree well with each other and display an enrichment in LREEs. As the main host phase for Th and U, their abundances obtained using LA-ICP-TOF-MS mapping, LA-spot analysis, and from literature values overlap with each other entirely.

Ca-rich pyroxene. The major element abundances determined using EPMA are in excellent agreement with literature values (ESI Table 6†). The average composition of Ca-rich pyroxene indicates the dominance of diopside (En$_{48}$Wo$_{46}$), which is also in excellent agreement with that observed for other H6 chondrites (En$_{49}$Wo$_{45}$).[48] In addition, the trace element abundances determined using LA-spot analysis overlap

378 | *J. Anal. At. Spectrom.*, 2023, **38**, 369–381

This journal is © The Royal Society of Chemistry 2023

within uncertainty with the literature values (ESI Table 6† and Fig. 7). Although the Fe abundances determined using LA-ICP-TOF-MS mapping are slightly affected by overlap with metal phases, most of the major element abundances for LA-ICP-TOF-MS mapping agree with the literature values. The trace element abundances for LA-ICP-TOF-MS mapping overall overlap both with those determined for LA-spot analysis and the literature values. Characterized by LREEs depletions and negative Eu anomalies, the CI-normalized REE patterns for LA-ICP-TOF-MS mapping, LA-spot analysis, and literature values are in good agreement as well, although negative Eu anomalies cannot be detected using LA-ICP-TOF-MS mapping due to the Eu abundances being below the LOD. However, the Ba, Th, and U abundances based on LA-ICP-TOF-MS mapping are ~2 to 5 times higher than those for LA-spot analysis. These discrepancies are likely the result of concentrations in Ca-rich pyroxene that are too close to the LODs. Remarkably, the Ce abundance in Y-790960 for LA-ICP-TOF-MS mapping is anomalously high and the CI-normalized REE pattern displays a strong positive Ce anomaly.

Feldspar. The major element abundances determined using EPMA are in excellent agreement with their literature values (ESI Table 7†). The average composition of feldspar indicates the presence of plagioclase, and albite ($Ab_{85}An_{10}$) more specifically. This is consistent with published values ($Ab_{82}An_{12}$).[48] The trace element abundances determined using LA-spot analysis overlap within uncertainty with the literature values, although those of HREEs in A 09618 are fairly low (ESI Table 7† and Fig. 7). In contrast, the abundances of both major and trace elements determined using LA-ICP-TOF-MS mapping are inconsistent with those determined using spot analyses and the literature values, except for elements concentrated in feldspar (*e.g.*, Na, Si, and K for major elements and Rb, Ba, and Eu for trace elements). This suggests that the effect of overlap with other phases during LA-ICP-TOF-MS mapping of feldspar is larger than for the other phases, since most feldspar grains co-exist complicatedly with Ca-rich pyroxene grains based on the petrographic observation. This is illustrated by anomalously high Mg abundances (% m m^{-1} level), as this element should only be present at the trace level in feldspar.

Low-Ca pyroxene. The major element abundances as determined using LA-ICP-TOF-MS mapping and EPMA are in good agreement with the literature values (ESI Table 8†). Note that the literature values represent the mean values of major elements in low-Ca pyroxene for L6 and LL6 chondrites but not for H chondrites, resulting in slight differences in the MgO and FeO contents. The average composition of low-Ca pyroxene in H chondrites published is $En_{82}Fs_{17}$, in agreement with that obtained using EPMA ($En_{82}Fs_{17}$).[48] In terms of trace elements (ESI Table 8† and Fig. 7), the values determined using LA-spot analysis approximately overlap within uncertainty with the literature values, except in the case of Sr and Ba where the literature values are apparently affected by contamination of feldspar. In addition, the CI-normalized REE patterns are mostly similar to those reported in the literature, all displaying increasing values from the LREEs to the HREEs with a negative Eu anomaly, except in the case of A 09618 where the Eu

abundance was not determined. Overall, the LREE abundances as obtained using LA-spot analysis are lower than the literature values. On the other hand, the signals for REEs obtained using LA-ICP-TOF-MS are mostly below the LODs. In addition, the Rb abundances exhibit a large discrepancy with the values based on LA-spot analysis and the literature values. These high Rb abundances can be due to the overlap with other phases, especially feldspar, as the Sr and Ba abundances are also higher than those determined using LA-spot analysis.

Olivine. Similar to low-Ca pyroxene, the MgO and FeO contents reported in literature differ from those obtained in this study. Except for these elements, most other major element abundances determined using LA-ICP-TOF-MS mapping and EPMA analysis overlap within uncertainty with the literature values (ESI Table 9†). The average composition of olivine obtained using EPMA is magnesium-rich (Fo_{81}) and in good agreement with values observed in other H6 chondrites (Fo_{81}).[48] Although many trace elements cannot be quantified using LA-ICP-TOF-MS mapping due their signals being below the LODs, at least, the Mn, Cu, and Zn abundances overall agree within uncertainty with the literature values (ESI Table 9† and Fig. 7). However, the abundances of the other elements quantified using LA-ICP-TOF-MS mapping appear to be elevated, likely as the result of overlap with other phases.

Oxides. Although the determinations of trace element abundances using LA-ICP-TOF-MS mapping and LA-spot analysis were focused primarily on Ca-phosphate and silicate phases, determination relying on LA-ICP-TOF-MS mapping was also applied to oxide phases. As such, LA-spot analysis was not conducted on oxide phases and the only abundances of trace elements available in literature or concentrated in the oxide phase are listed in ESI Table 10.† Overall, the major and trace element abundances determined in oxide phases agree within uncertainty with the literature values and those determined using EPMA, although no literature values for trace elements in ilmenite exist. Only a single grain of ilmenite, which is relatively large with ~100 μm for the major axis and ~50 μm for the minor axis, was found in the LA-ICP-TOF-MS maps (Fig. 5(c)) and analyzed, and hence the elemental abundances of ilmenite, particularly for the trace elements, may not reflect representative values.

In summary, the elemental abundances in each phase determined using fast high-resolution LA-ICP-TOF-MS mapping with a 5 × 5 μm spot size are mostly in agreement with the comparison values, although conventional EPMA and LA-spot analysis are generally more accurate and precise for major elements and trace elements, respectively, than LA-ICP-TOF-MS mapping. Especially for the elements in their main host phase(s), *i.e.*, REEs in Ca-phosphates, Th and U in apatite, Sc and Hf in Ca-rich pyroxene, *etc.*, LA-ICP-TOF-MS mapping can be used to obtain quantitative data that are approaching the accuracy of those obtained by spot analyses. However, the lower the elemental abundances in the phases are, the larger the discrepancy between those values obtained using LA-ICP-TOF-MS mapping and the comparison values in general is. For example, it is challenging to quantify or even detect the REEs when the abundances of the REEs in the target phase are

This journal is © The Royal Society of Chemistry 2023

J. Anal. At. Spectrom., 2023, **38**, 369–381 | **379**

present at a concentration level similar to or lower than those of bulk chondrites. In general, elemental abundances in the target phase at least at the $\mu g\ g^{-1}$ level are required for the quantification of LA-ICP-TOF-MS mapping to be at similar accuracy to those obtained by other, more conventional quantitative techniques, although levels at hundreds of $ng\ g^{-1}$ may be quantified in the case of heavy elements, from the HREEs onwards.

Conclusions

Fast elemental mapping using LA-ICP-TOF-MS was applied to H chondrites with the aim of obtaining element maps for a large collection of elements, including trace elements. The merits of quantification were assessed by comparison of the data obtained with those obtained using more conventional approaches, such as spot drilling analysis using LA-ICP-SF-MS, in an attempt to examine to what extent the accuracy and precision of the data obtained using this fast elemental mapping can approach those of more conventional analysis. A number of limitations for LA-ICP-TOF-MS mapping applying the experimental conditions used in this study (4.00 J cm^{-2} laser energy density, 5×5 μm spot size, up to 200 pixel per s, *etc.*) are identified: pure metal phases which are not oxidized or hydrated due to terrestrial weathering cannot be ablated effectively, and the minimum abundances for trace elements required in terms of quantification are considerably higher than those for LA-spot analysis (*i.e.*, at the level of several of $\mu g\ g^{-1}$ for LA-ICP-TOF-MS mapping *vs.* several $ng\ g^{-1}$ level for LA-spot analysis). However, the trace element maps provide information on elemental distributions among the constituent minerals (semi-)quantitatively, especially for their primary host phase(s), and demonstrate the value of this technique to obtain high-resolution spatially resolved information without any stringent sample preparation, as is the case for more conventional techniques. Importantly, the approach applied in this study led to the identification of unexpected trace element carrier phases, on which almost no study focusing on trace elements has been conducted so far (*e.g.*, REEs in cracks, V and Zn in chromite, and Nb and Ta in ilmenite). Because no ablation effects in the regions studied using LA-ICP-TOF-MS mapping are observed based on the BSE imaging, EPMA, and LA-spot analysis, this fast LA-ICP-TOF-MS mapping can be used as a screening tool for particular geological samples and possibly also other types of samples (*e.g.*, archeological artefacts), providing (semi-)quantitative information of elemental distributions including trace elements on such samples.

Conflicts of interest

There are no conflicts to declare.

Acknowledgements

References

1 C. A. Heinrich, T. Pettke, W. E. Halter, M. Aigner-Torres, A. Audétat, D. Günther, B. Hattendorf, D. Bleiner, M. Guillong and I. Horn, *Geochim. Cosmochim. Acta*, 2003, **67**, 3473–3497.

2 K. P. Jochum, B. Stoll, K. Herwig and M. Willbold, *J. Anal. At. Spectrom.*, 2007, **22**, 112–121.

3 M. Humayun, F. A. Davis and M. M. Hirschmann, *J. Anal. At. Spectrom.*, 2010, **25**, 998–1005.

4 J. D. Woodhead, J. Hellstrom, J. M. Hergt, A. Greig and R. Maas, *Geostand. Geoanal. Res.*, 2007, **31**, 331–343.

5 T. Ulrich, B. S. Kamber, P. J. Jugo and D. K. Tinkham, *Can. Mineral.*, 2009, **47**, 1001–1012.

6 S. J. M. Van Malderen, J. T. van Elteren and F. Vanhaecke, *J. Anal. At. Spectrom.*, 2015, **30**, 119–125.

7 S. J. M. Van Malderen, A. J. Managh, B. L. Sharp and F. Vanhaecke, *J. Anal. At. Spectrom.*, 2016, **31**, 423–439.

8 O. Borovinskaya, B. Hattendorf, M. Tanner, S. Gschwind and D. Günther, *J. Anal. At. Spectrom.*, 2013, **28**, 226–233.

9 L. Hendriks, A. Gundlach-Graham, B. Hattendorf and D. Günther, *J. Anal. At. Spectrom.*, 2017, **32**, 548–561.

10 A. Gundlach-Graham, P. S. Garofalo, G. Schwarz, D. Redi and D. Günther, *Geostand. Geoanal. Res.*, 2018, **42**, 559–574.

11 T. Stephan, *Planet. Space Sci.*, 2001, **49**, 859–906.

12 M. Morita, M. Miyamura, A. Yamaguchi and T. Sakamoto, *Anal. Sci.*, 2022, 1–8.

13 A. N. Krot, K. Keil, C. A. Goodrich, E. R. D. Scott and M. K. Weisberg, *Meteorites, Comets, and Planets Treatise on Geochemistry*, 2003, vol. 341, pp. 83–128.

14 M. Burger, G. Schwarz, A. Gundlach-Graham, D. Käser, B. Hattendorf and D. Günther, *J. Anal. At. Spectrom.*, 2017, **32**, 1946–1959.

15 A. Gundlach-Graham, M. Burger, S. Allner, G. Schwarz, H. A. O. Wang, L. Gyr, D. Grolimund, B. Hattendorf and D. Günther, *Anal. Chem.*, 2015, **87**, 8250–8258.

380 | *J. Anal. At. Spectrom.*, 2023, **38**, 369–381

This journal is © The Royal Society of Chemistry 2023

16 Y. Bussweiler, O. Borovinskaya and M. Tanner, *Spectroscopy*, 2017, **32**, 14–20.

17 M. Y. Krebs, D. G. Pearson, A. J. Fagan, Y. Bussweiler and C. Sarkar, *Chem. Geol.*, 2019, **523**, 42–58.

18 T. Ubide, J. Caulfield, C. Brandt, Y. Bussweiler, S. Mollo, F. Di Stefano, M. Nazzari and P. Scarlato, *Front. Earth Sci.*, 2019, **7**, 239.

19 Y. Bussweiler, F. Gervasoni, M. Rittner, J. Berndt and S. Klemme, *Lithos*, 2020, **352–353**, 105282.

20 C. Neff, P. Keresztes Schmidt, P. S. Garofalo, G. Schwarz and D. Günther, *J. Anal. At. Spectrom.*, 2020, **35**, 2255–2266.

21 D. Rubatto, M. Burger, P. Lanari, B. Hattendorf, G. Schwarz, C. Neff, P. Keresztes Schmidt, J. Hermann, A. Vho and D. Günther, *Contrib. Mineral. Petrol.*, 2020, **175**, 1–19.

22 M. W. Förster, Y. Bussweiler, D. Prelević, N. R. Daczko, S. Buhre, R. Mertz-Kraus and S. F. Foley, *Geosciences*, 2021, **11**, 372.

23 P. S. Garofalo, M. Scarsi, A. Gundlach-Graham, G. Schwarz and D. Günther, *Miner. Deposita*, 2022, 1–20.

24 R. Maeda, S. Goderis, V. Debaille, H. Pourkhorsandi, G. Hublet and P. Claeys, *Geochim. Cosmochim. Acta*, 2021, **305**, 106–129.

25 K. Ninagawa, Y. Mieda, H. Ueda, N. Imae, H. Kojima and K. Yanai, *Antarct. Meteorite Res.*, 2005, **18**, 1–16.

26 S. J. M. Van Malderen, T. Van Acker and F. Vanhaecke, *Anal. Chem.*, 2020, **92**, 5756–5764.

27 F. Vanhaecke and S. J. M. Van Malderen, European Patent, No. 3195346B1, European Patent Office, Munich, Germany, 2020.

28 T. Van Acker, S. J. M. Van Malderen, T. Van Helden, C. Stremtan, M. Šala, J. T. van Elteren and F. Vanhaecke, *J. Anal. At. Spectrom.*, 2021, **36**, 1201–1209.

29 M. Burger, A. Gundlach-Graham, S. Allner, G. Schwarz, H. A. Wang, L. Gyr, S. Burgener, B. Hattendorf, D. Grolimund and D. Güther, *Anal. Chem.*, 2015, **87**, 8259–8267.

30 M. J. Cubison and J. L. Jimenez, *Atmos. Meas. Tech.*, 2015, **8**, 2333–2345.

31 J. T. van Elteren, N. H. Tennent and V. S. Šelih, *Anal. Chim. Acta*, 2009, **644**, 1–9.

32 M. Humayun, S. B. Simon and L. Grossman, *Geochim. Cosmochim. Acta*, 2007, **71**, 4609–4627.

33 M. Tanner, *J. Anal. At. Spectrom.*, 2010, **25**, 405–407.

34 K. P. Jochum, M. Willbold, I. Raczek, B. Stoll and K. Herwig, *Geostand. Geoanal. Res.*, 2005, **29**, 285–302.

35 K. P. Jochum, B. Stoll, K. P. Herwig, M. Willbold, A. W. Hofmann, M. Amini, *et al.*, *Geochem., Geophys., Geosyst.*, 2006, **7**, Q02008.

36 M. A. W. Marks, T. Wenzel, M. J. Whitehouse, M. Loose, T. Zack, M. Barth, L. Worgard, V. Krasz, G. N. Eby, H. Stosnach and G. Markl, *Chem. Geol.*, 2012, **291**, 241–255.

37 L.-K. Sha and W. Chappell, *Geochim. Cosmochim. Acta*, 1999, **63**, 3861–3881.

38 A. Yamaguchi, N. Shirai, M. Kimura, N. Imae, M. Haba, V. Debaille, R. Maeda, S. Goderis and P. Claeys, *Meteorite Newsletter*, 2021, vol. 28.

39 B. Mason and A. L. Graham, *Earth Sci.*, 1970, **3**, 1–17.

40 D. B. Curtis and R. A. Schmitt, *Geochim. Cosmochim. Acta*, 1979, **43**, 1091–1103.

41 T. H. Green, *Chem. Geol.*, 1994, **117**, 1–36.

42 D. Ward, A. Bischoff, J. Roszjar and M. J. Whitehouse, *Am. Mineral.*, 2017, **102**, 1856–1880.

43 M. Ebihara and M. Honda, *Meteoritics*, 1984, **19**, 69–77.

44 J. T. Wasson and G. W. Kallemeyn, *Philos. Trans. R. Soc. Lond.*, 1988, **A325**, 535–544.

45 R. O. Allen Jr and B. Mason, *Geochim. Cosmochim. Acta*, 1973, **37**, 1435–1456.

46 D. B. Curtis, PhD thesis, Oregon State University, Oregon, 1974.

47 E. Anders and N. Grevesse, *Geochim. Cosmochim. Acta*, 1989, **53**, 197–214.

48 W. R. Van Schmus, *Earth-Sci. Rev.*, 1969, **5**, 145–184.

This journal is © The Royal Society of Chemistry 2023

J. Anal. At. Spectrom., 2023, **38**, 369–381 | **381**